Applied Catalysis B: Environmental 282 (2021) 119572

Contents lists available at ScienceDirect

Applied Catalysis B: Environmental

journal homepage: www.elsevier.com/locate/apcatb

Electro-conversion of methane to alcohols on "capsule-like" binary metal oxide catalysts

Nengneng Xu[a,b,1], Cameron A. Coco[a,b,1], Yudong Wang[a,b], Tianshun Su[a,b], Yu Wang[a,c], Luwei Peng[d], Yanxing Zhang[a,e], Yuyu Liu[f], Jinli Qiao[d,**], Xiao-Dong Zhou[a,b,*]

[a] Institute for Materials Research and Innovation, University of Louisiana at Lafayette, Lafayette, LA 70504, United States
[b] Department of Chemical Engineering, University of Louisiana at Lafayette, Lafayette, LA 70504, United States
[c] Department of Chemistry, University of Louisiana at Lafayette, Lafayette, LA 70504, United States
[d] State Key Laboratory for Modification of Chemical Fibers and Polymer Materials, College of Environmental Science and Engineering, Donghua University, 2999 Ren'min North Road, Shanghai 201620, China
[e] College of Physics and Materials Science, Henan Normal University, Xinxiang, Henan 453007, China
[f] Institute for Sustainable Energy, College of Sciences, Shanghai University, Shanghai 200444, China

ARTICLE INFO

Keywords:
Binary metal oxide
CuO_x
Methane conversion
High activity
Alcohol

ABSTRACT

Research on the electro-conversion of methane has been driven by the necessity of addressing a key catalytic challenge to oxidize methane to liquid products at ambient conditions. In this work, we employed a series of binary metal oxide catalysts with capsule-like morphology by anchoring ZrO_2 on Cu oxide (CuO_x) for the oxidation of methane. The ZrO_2:$CuO_{x(180,\ 24)}$ was found to convert methane with a difference in current density up to 13.35 mA cm^{-2} in comparison with ZrO_2, CuO_x, and other ZrO_2:CuO_x. The density functional theory calculations show that the enhanced activity originated from the increased charge distribution in ZrO_2 after the ZrO_2 cluster grew on the $Cu_2O(111)$, which enhances the activity of CH_4 dissociation and improves the electronic conduction through Cu_2O support. Benefiting from these advantages, the hybrids exhibit a high catalytic activity and stability. Surprisingly, 1-propanol and 2-propanol were the main products after 18 -h operation under ambient conditions.

1. Introduction

In comparison with coal and petroleum, natural gas is the cleanest fossil fuel, and has become a primary energy source in both industrial processes and human daily life [1–3]. Methane (CH_4), a greenhouse gas, is the main component (85 %) of natural gas and its emission is more than 30 times more impactful on the environment than CO_2 [2,4,5]. The negative effect of CH_4 emissions has attracted growing attention due to the increasing energy demand and environmental pollution [6]. As a result, transformation of methane to other chemicals, for example, formaldehyde, methanol, and ethylene, is desired [7–9]. The electrochemical conversion of methane to alcohols is of particular interest because this process is capable of stabilizing the desirable intermediates and reducing the activation barriers of the charge transfer reaction. This can be accomplished through the proper selection of electrocatalysts and operating potentials. It is known that under the same conditions, electrochemical reactions are generally faster than the corresponding chemical reactions and therefore a significant effect on the slow reactions, such as the partial oxidation, can be expected (**Table S1**) [10–20]. Moreover, the electrochemical oxidation is capable of directly converting methane to liquid products at ambient conditions, which enables a possibly cost-effective process [11,12,21]. However, CH_4 is the least reactive of all the paraffin hydrocarbons, attributed to its high dissociation energy of C–H bonds (104 kcal mol^{-1}) [22]. Accordingly, CH_4 is not expected to be readily oxidized by O_2 to form singlet methanol by O_2 at room temperature [23]. Hence, it is necessary to use other suitable oxidizing agents [8]. Hydroxide has been used as the oxidizing agent to extract protons from CH4 in a traditional electrocatalytic system. However, hydroxide also exhibited negligible activity at room temperature. [24]. On the contrary, carbonate (CO_3^{2-}) ions provide an attractive feature by offering a charged oxygen atom via the reaction of $CO_3^{2-} \leftrightarrow CO_2 + O^{2-}$ under mild conditions [25,26]. The O^{2-}

* Corresponding author at: Institute for Materials Research and Innovation, University of Louisiana at Lafayette, Lafayette, LA 70504, United States.
** Corresponding author.
E-mail addresses: qiaojl@dhu.edu.cn (J. Qiao), zhou@louisiana.edu (X.-D. Zhou).
[1] Equal contribution.

https://doi.org/10.1016/j.apcatb.2020.119572
Received 24 July 2020; Received in revised form 19 September 2020; Accepted 20 September 2020
Available online 23 September 2020

generated in the liquid medium can lower the reaction barrier and accelerate the kinetics of methane oxidation reaction (MOR). Therefore, the electrocatalyst must exhibit the ability towards CO_3^{2-} adsorption on its surface. Zirconia (ZrO_2) has rich Lewis acid active sites and electron acceptability, showing a remarkable adsorption capacity of CO_3^{2-} [27,28]. Based on these characteristics, zirconia-based hybrids have attracted growing attention as an electrocatalyst. Primarily, transition metal oxide (TMO), such as NiO and Co_3O_4, doped ZrO_2 to form TMO/ZrO_2. These compounds showed the potential for methane oxidation at room temperature [25,29,30]. However, the TMO/ZrO_2 hybrid still faces the following issues: (i) a low activity and selectivity with sluggish kinetics and many side chemical reactions; (ii) poor stability attributed to the weak contact between TMO and ZrO_2, and (iii) an unclear reaction mechanism. Therefore, further developing highly efficient TMO/ZrO_2 electrocatalysts and studying their reaction mechanisms are needed to understand and improve CH_4 oxidation processes.

Compared to NiO and Co_3O_4, copper-based (Cu) catalysts have a high activity and a long-term durability on forming the liquid and gas organics of a C1 catalysis reaction system (CO_2 reduction reaction) at room temperature [31–35]. In addition, CuO_x shows good adsorption for CH_4 and methanol [36–38]. According to theoretical calculations, methanol can be further oxidized to form ethanol on the oxide surface, illustrating the high selectivity of a Cu-based catalyst towards the formation of higher alcohols [39,40]. Hence, it becomes more attractive to utilize a highly efficient MOR electrocatalyst consisting of CuO_x and ZrO_2 [41–43]. The advantages of this type of catalytic structure include: (i) a possibly high activity and fast intrinsic kinetics due to the coupling effect between Cu oxides and Zr oxides; (ii) long-term stability which is attributed to the formation of the stable ZrO_2/CuO_x binary metal oxide structure; (iii) the promotion for CH_4 dissociation resulting from the charge redistribution; and (iv) high electronic conduction by forming a new electron transfer pathway. Notably, a CuO_x-adsorbing ZrO_2 hybrid has not yet been studied in the electrochemical oxidation of methane.

Inspired by the above advantages, we synthesized a series of capsule-like ZrO_2:CuO_x hybrid catalysts to enhance methane oxidation activity at room temperature in this work. To the best of our knowledge, this hybrid is a new electrocatalyst for the selective electrochemical oxidation of methane to produce propanol (1-propanol and 2-propanol). Comparative experimental investigation illustrates the strong synergistic effect between CuO_x and ZrO_2, which its unique catalytic structure and electron transfer pathway are responsible for accelerating electrochemical activity. Density function theory (DFT) calculations reveal an obvious charge redistribution after the ZrO_2 anchored on the Cu_2O(111), which enhances the CH_4 dissociation and forms a quick electron transfer network. Consequently, the ZrO_2:CuO_x manifests high activity with a large current difference of 13.35 mA cm^{-2} and long-time durability with almost no change in performance for 40 h, surpassing many of the recently reported catalysts. Notably, high levels of 1-propanol (2105.8 ug mL^{-1}) and 2-propanol (2084.8 ug mL^{-1}) as the main alcohol products were collected after 18 h, with a production efficiency > 56 %. Hence, the study reported herein may encourage research on the design of other new high-activity and robust binary metal oxides; TMO-based electrocatalysts for the oxidation of methane at room temperature.

2. Experiment section

2.1. Preparation of CH_4 oxidation catalysts

The ZrO_2:CuO_x powders were synthesized from the hydrothermal method. Initially, 2 mmol $Cu(CH_3COO)_2$ $4H_2O$ and 2 mmol $ZrOCl_2$ H_2O were dissolved in 60 mL deionized (DI) water. Then, 14.4 g NaOH were added into the Zr and Cu ion solution, with vigorous stirring for 1 h. Next, the as-prepared solution was transferred to a 100 mL container and heated at 180 °C for 24 h. After the hydrothermal treatment, the precipitant was collected after being rinsed and centrifuged with DI water 3 times and isopropanol 1 time, respectively. The collected and clean powders were dried at 70 °C for 6 h. Finally, the sample was annealed at 350 °C in air for 1 h to convert it into the ZrO_2:CuO_x composite (denoted as ZrO_2:$CuO_{x(180,24)}$). The 0.5 g ZrO_2:$CuO_{x(180,\ 24)}$ was treated in 40 mL 0.1 M H_2SO_4, with stirring for 2 h. The H_2SO_4-treated powders were collected after being washed and centrifuged with DI water 3 times and isopropanol 1 time, respectively, then were dried at 70 °C for 6 h to form the final specimen (denoted as ZrO_2:$CuO_{x(180,24)\text{-}acid}$). For comparison, ZrO_2:$CuO_{x(180,24)}$ powders, such as ZrO_2:$CuO_{x(180,12)}$, ZrO_2:$CuO_{x(180,18)}$, and ZrO_2:$CuO_{x(180,30)}$, were prepared by the same synthesizing method as ZrO_2:CuO_x at 12 h, 18 h and 30 h instead of 24 h, respectively. Additionally, pure ZrO_2 and CuO_x were synthesized without $Cu(CH_3COO)_2$ $4H_2O$ and 2 mmol $ZrOCl_2$ H_2O, respectively.

2.2. Physical characterization

Morphology and structure analyses of these samples were employed by using X-ray diffraction (XRD, Philips PW3830, Cu Kα radiation and λ = 1.5406 Å), scanning electron microscope (SEM, Hitachi S3600), and high-resolution TEM (HRTEM, JEOL 2010 F, 200 kV) measurements. EDS spectra and mapping were conducted for obtaining the elements ratio and distribution measurement. X-ray photoelectron spectroscopy (XPS, Thermo Scientific with an A1 Ka X-ray source) analysis was carried out for further analysis of the physical structure. The methane oxidation products were recorded by ^{1}H-NMR (Varian MR 400 MHz NMR spectrometer) and GC–MS instrument (Agilent 7890A/5975C).

2.3. Electrochemical measurements

Liner scanning voltammetry (LSV) and electrochemical impedance spectroscopy (EIS) of these samples were performed in a standard half-cell system using Solartron 1470E Multistat and 1255B Frequency Response Analyzer (Solartron Analytical, Oak Ridge, TN, 37830) with Ag/AgCl electrode as the reference electrode, platinum (Pt) wire as the counter electrode, and a glassy carbon electrode with catalyst as working electrode. 0.5 M Na_2CO_3 was used as the electrolyte. In detail, all working electrodes were obtained by dropping 16 μL of 5 mg mL^{-1} catalyst ink (powder samples in isopropanol (4.98 mL) and Nafion@ solution (20 μL)) on the surface of the glassy carbon area (0.19625 cm^2). Ultra-high purity methane gas and nitrogen gas were bubbled in the electrolyte for 1 h before each test. LSV was obtained in CH_4-saturated and N_2-saturated electrolyte at 5 mV s^{-1} with the potential range for 0 V to 1.3 V vs. Ag/AgCl, respectively. EIS performances were obtained in a frequency range from 0.1–100 kHz with a perturbation of 10 mV. In addition, the long-term electrochemical oxidation of CH_4 was carried out in a three-electrode system. The Pt foil and Ag/AgCl electrode were used as the counter electrode and reference electrode, respectively. The carbon paper with the loading of 2 mg cm^{-2} was prepared by spraying the sample ink on the surface as working electrode, which was used for home-made reactor assembling. The sample ink was obtained by dispersing 25 mg of sample powder in 10 mL mixture solution of 9.8 mL isopropanol and 0.2 mL 5% Nafion@ solution with ultrasonic treatment for half an hour.

3. Results and discussion

3.1. Synthesis and characterization

The ZrO_2:CuO_x hybrid was prepared by one-step hydrothermal and calcination methods (Fig. 1**(a)**). In addition, pure CuO_x and pure ZrO_2 were synthesized for comparison. As shown in **Figure S1(a)**, the CuO_x sample is composed of Cu_2O (JCPDS: 43-0953) and CuO (JCPDS: 44-0706), with the Cu^{2+}/Cu^{+} ratio being 79:21. The pure ZrO_2 corresponds to the monoclinic structure (JCPDS: 37-1484, **Figure S1(b)**).

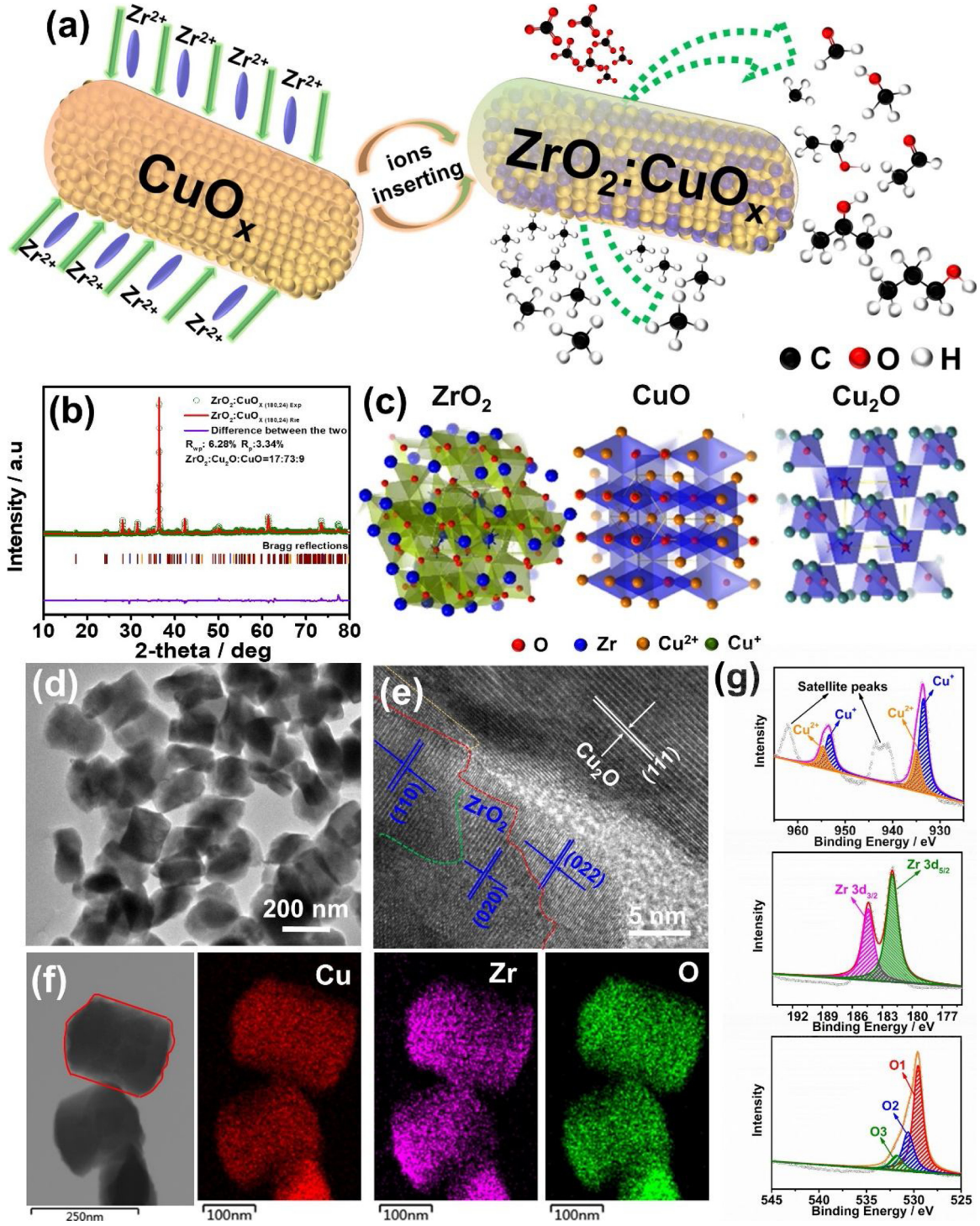

Fig. 1. (a) The fabrication process of the ZrO_2:CuO_x hybrid catalyst and its CH_4 electrochemical oxidation, (b) the observed, calculated, and difference profiles from XRD data for ZrO_2:$CuO_{x(180,24)}$, (c) Crystal structures of ZrO_2, CuO, and Cu_2O, (d) TEM image of ZrO_2: $CuO_{(180,24)}$, (e) HRTEM image of ZrO_2:$CuO_{x(180,24)}$, (f) TEM image and element mapping of ZrO_2:$CuO_{x(180,24)}$, (g) deconvoluted Cu 2p, Zr 3d and O 1s XPS signals of ZrO_2:$CuO_{x(180,24)}$.

TEM images reveal a leaf-like ZrO_2 with the size of 400 μm (**Figure S2(a)** and **(b)**). The CuO_x sample shows sheet-like morphology and the large particles are more than 600 μm in size (**Figure S2(c)** and **(d)**). Hence, the XRD, TEM, and XPS were carried out to further observe the structure, morphology, and chemical state of different samples synthesized using different hydrothermal times, denoted as ZrO_2:$CuO_{(180,12)}$, ZrO_2:$CuO_{(180,18)}$, ZrO_2:$CuO_{(180,24)}$, and ZrO_2:$CuO_{(180,30)}$. Compared with ZrO_2 and CuO_x, all diffraction peaks of the ZrO_2:CuO_x correspond to the related peaks of ZrO_2, Cu_2O, and CuO (Figs. 1**(b)** and **S3**). Among all samples, the typical planes of ZrO_2 did not apparently shift and were displayed at 17.4° (001), 24.1° (110), 24.4° (011), 28.2° (-111), 31.2° (111), 34.4° (020), and 50.1° (022), respectively. In contrast, the typical (111) planes of Cu_2O at 36.5° show obvious changes. The peak gradually increases in intensity as the hydrothermal time increases up to 24 h. It is worth noting that the ratio of ZrO_2, Cu_2O, and CuO in the hybrid varies with reaction time. The mass ratio of the ZrO_2 remains almost constant at 18 % after 12 h. However, the mass ratio of the Cu_2O shows a different trend. At 24 h, the

ZrO_2:$CuO_{(180,24)}$ illustrates the biggest mass ratio of the Cu_2O of 71 %, and the smallest mass ratio of the CuO of 12 %. These findings reveal that the component of CuO_x in the ZrO_2:$CuO_{x(180,24)}$ is almost Cu_2O. The mass ratio of ZrO_2:CuO_x will be further supported by TEM-Mapping and XPS. In addition, the morphology of all ZrO_2:CuO_x samples were observed by TEM.

In all samples, ZrO_2 nanoparticles uniformly grew into the CuO_x, forming the unique capsule-like ZrO_2:CuO_x hybrid (Figs. 1**(d)**, **S4(a)**, **S5(a)**, and **S6(a)**). Before 18 h, the ZrO_2 nanoparticles can be easily distinguished from CuOx nanoparticles. The CuO_x sheets are surrounded by ZrO_2 leaves, where ZrO_2 is gradually embedded into the CuO_x. Upon further increasing the time of hydrothermal processing, the morphology and size of these hybrids show almost no change while the ZrO_2:CuO_x show different crystal structures with different exposed planes. From the HRTEM image (Fig. 1**(e)**), the lattice spacing of ZrO_2 are 0.369 nm, 0.261 nm, and 0.187 nm, corresponding to (110), (020), and (022) facets, respectively. The lattice spacing of CuO_x is 0.248 nm, corresponding to the (111) plane. For ZrO_2:$CuO_{x(180,12)}$, the lattice spacings are 0.187 nm and 0.248 nm, corresponding to (022) facet of ZrO_2 and (110) facet of CuO_x, respectively (**Figure S4(b)**). For ZrO_2:$CuO_{x(180,18)}$, the (111) plane of CuO_x is found in **Figure S5(b)**. In addition, ZrO_2:$CuO_{x(180,30)}$ also shows the (020) plane of ZrO_2 (**Figure S6(b)**). In order to further analyze the distribution and ratio of the Zr, Cu, and O atoms, elemental mapping and EDS were applied (Figs. 1**f** and **S4c-S6c)**. From these results, the ZrO_2 and CuO_x are confirmed to be uniformly distributed. Specifically, the elemental distribution of ZrO_2:CuO_x is almost unchanged. However, the ratio of ZrO_2:CuO_x was well in agreement with the refined XRD results. It further proved the Cu_2O is the main component of ZrO_2:$CuO_{(180,18)}$. From the XRD pattern and TEM images, uniform distribution and strong physical connection between CuO_x and ZrO_2 could be revealed and lead to the synergistic effect, which may be beneficial to the catalytic activity of CH_4 oxidation.

XPS measurement was carried out to provide further evidence. As shown in Figs. 1**(g)** and **S7**, Cu 2p signals, Zr 3d signals, and O 1s signals, along with survey scans, were obtained for ZrO_2:CuO_x. The binding energy of Cu core levels did not clearly shift upon changing the hydrothermal time past 18 h. The Cu 2p spectra of ZrO_2:$CuO_{x(180,18)}$ has a right shift, which may be attributed to the electron transformation from Cu^{2+} to Cu^+ and from Cu ions to Zr ions. In Fig. 1**(g)**, the Cu 2p spectrum shows Cu $2p_{3/2}$, Cu $2p_{1/2}$, and 2 satellite peaks. The Cu $2p_{3/2}$ and Cu $2p_{1/2}$ peaks are deconvoluted into 4 peaks. The deconvoluted peaks at around 933.5 eV and 934.8 eV are assigned to Cu^+ species and Cu^{2+} species, respectively [44,45]. For Zr 3d spectra, its intensity and location are clearly changed as the reaction time increases. Actually, this shift to the right corresponds to the process by which CuO_x adsorbs ZrO_2 [46]. At 12 h, a majority of ZrO_2 was adsorbed on the top CuO_x surface, while a small number of ZrO_2 inserted into the CuO_x. As time increases, the proportion of ZrO_2 in the mixture increases, which leads to the electron transition from CuO_x to ZrO_2, achieving a Cu^+ conversion [47]. It is beneficial to expose more active sites and improve the conductivity. For 30 h, a further increase of the Cu content in the sample results in the partial migration of electrons from ZrO_2 to Cu_2O, which decreases the number of Cu active sites. Additionally, the O 1s spectrum was deconvoluted into 3 peaks, which can be indexed to the lattice oxygen (O1, 529.5 eV), the oxygen vacancies (O2, 530.5 eV), and the number of defect sites (O3, 532.1 eV), respectively [48,49]. Compared to other ZrO_2:CuO_x, ZrO_2:$CuO_{x(180,24)}$ has a higher intensity of O1 and O3, implying more active sites and the ability of ZrO_2 to enhance surface charge adsorption, respectively. These changes reveal the ZrO_2:CuO_x crystal state is affected and results in higher CH_4 oxidation performance of ZrO_2:$CuO_{(180,24)}$, which match the results of XRD and TEM well.

3.2. Electrochemical performance

To measure the electrocatalytic performance of MOR at room temperature, a 3-electrode electrochemical system was assembled with a Pt wire as the counter electrode, a Ag/AgCl electrode as the reference electrode, a catalyst-loaded glassy carbon electrode as the working electrode, and 0.5 M carbonate solution as the electrolyte. Figs. 2**(a)-(c)** show the linear sweep voltammetry (LSV) curves of ZrO_2:$CuO_{x(180,24)}$, ZrO_2 and CuO_x in CH_4, and N_2-saturated carbonate electrolyte, respectively. The oxidation current should be attributed to oxygen evolution reaction (OER) and CH_4 oxidation reaction (MOR). The current density in N_2-saturated carbonate electrolyte should be caused by OER.

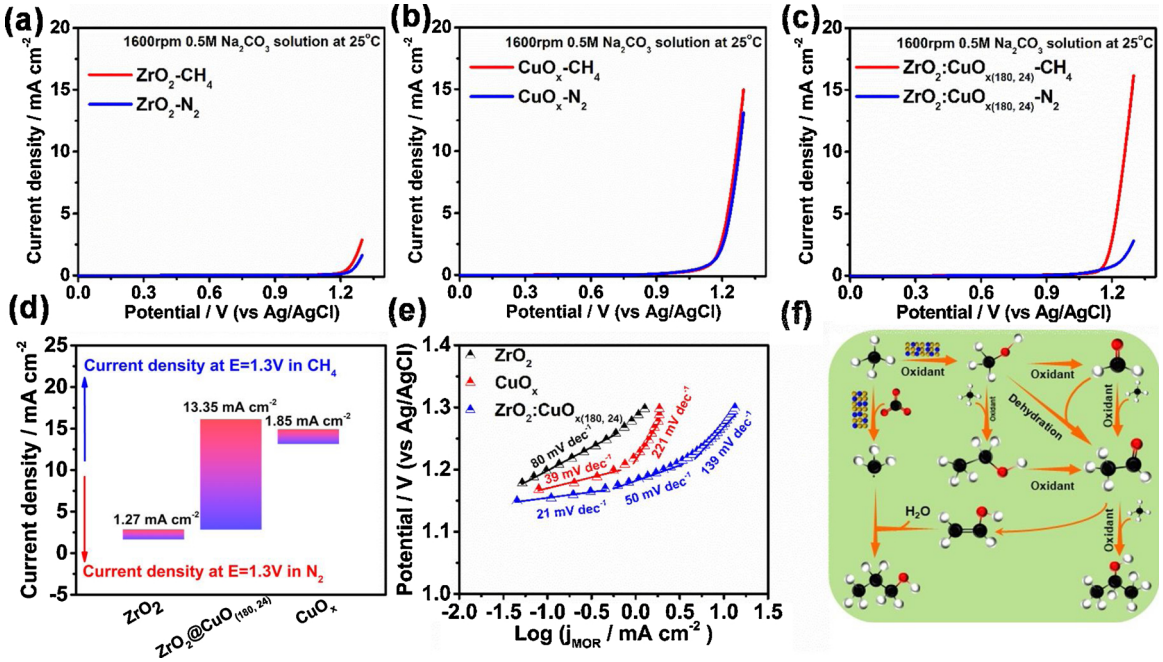

Fig. 2. LSV curves of (a) ZrO_2, (b) CuO_x, and (c) ZrO_2:$CuO_{x(180,24)}$ in CH_4 and N_2-saturated carbonate electrolyte, respectively; (d) the current density difference Δj of ZrO_2, CuO_x, and ZrO_2:$CuO_{x(180,24)}$; (e) Tafel slope of ZrO_2, CuO_x, and ZrO_2:$CuO_{x(180,24)}$; (f) schematic of MOR mechanism.

Hence, the current density difference (Δj, mA cm^{-2}) of catalyst between CH_4- and N_2-saturated carbonate electrolytes is a key parameter to evaluate the catalytic activity of MOR. The ZrO_2:$CuO_{x(180,24)}$ exhibited a large Δj of 13.35 mA cm^{-2}, which is 10 and 7 times greater than that of ZrO_2 (1.27 mA cm^{-2}) and CuO_x (1.85 mA cm^{-2}), respectively (Fig. 2**(d)**). The result not only proves the high MOR activity, but also reveals the strong synergistic effect between ZrO_2 and CuO_x. In detail, the ZrO_2 displayed a low activity for both CH_4- and N_2-saturated electrolytes, while the CuO_x showed high OER activity. Hence, the strong synergistic effect could further enhance the MOR activity with considerably suppressed side reaction of OER. In addition, the high performance may be attributed to the good conductivity, which can be further observed via electrochemical impedance spectroscopy (EIS). **Figures S8** illustrates the EIS results of these samples, which is well in agreement with the LSV discussion. The ZrO_2:$CuO_{x(180,24)}$ has good electronic conduction and a lower ohmic resistance (~ 20.7 Ω) for MOR than ZrO_2 (~ 22.7 Ω) and CuO_x (~ 21.8 Ω). Notably, the ZrO_2:$CuO_{x(180,24)}$ demonstrated a lower charge-transfer resistance with CH_4-saturated electrolyte than ZrO_2:$CuO_{(180,12)}$, ZrO_2:$CuO_{(180,24)}$, and ZrO_2:$CuO_{(180,30)}$, which in turn results in fast kinetics and a highly efficient transfer pathway of MOR. Compared with other ZrO_2:CuO_x, the ZrO_2:$CuO_{(180,24)}$ exhibits more promising performance with a larger Δj and lower resistance than ZrO_2:$CuO_{(180,12)}$, ZrO_2:$CuO_{(180,18)}$, and ZrO_2:$CuO_{(180,30)}$. Combined with the results of physical characterization (XRD, XPS, and TEM), it can be found that the activity of the catalyst is related to CuO_x in the sample, particularly Cu_2O. The higher the Cu_2O proportion in the hybrid, the better the MOR activity of the sample. Meanwhile, the (111) crystal plane is beneficial to the electrocatalytic process. To further study the active sites of the hybrid, the ZrO_2:$CuO_{x(180,24)}$ was soaked in sulfuric acid for 2 h to remove CuO_x from the sample, which is denoted as ZrO_2:$CuO_{x(180,24)\text{-acid}}$. In this regard, the main ingredient of the ZrO_2:$CuO_{x(180,24)\text{-acid}}$ is ZrO_2 (**Figure S9(a)**). Compared with pure ZrO_2, the ZrO_2:$CuO_{x(180,24)\text{-acid}}$ shows a different structure, but has a similar morphology to, ZrO_2:$CuO_{x(180,24)}$ (**Figures S9(a–c)**). Importantly, the low catalytic activity of ZrO_2:$CuO_{x(180,24)\text{-acid}}$ is the same as the pure ZrO_2 (**Figure S9(d)**), further confirming that the CuO_x plays a pivotal role in the active site of the hybrid. Moreover, the ZrO_2:$CuO_{x(180,24)}$ also manifests a clearly enhanced stability when compared to ZrO_2:$CuO_{(180,12)}$, ZrO_2:$CuO_{(180,18)}$, and ZrO_2:$CuO_{(180,30)}$ (**Figure S10**).

Tafel analysis was carried out to further study the kinetic mechanism of MOR on the ZrO_2:$CuO_{x(180,24)}$ catalyst, (Fig. 2**e**) including pure CuO_x and pure ZrO_2. In the linear Tafel region, pure ZrO_2 exhibited a Tafel slope of 80 mV dec^{-1}, indicating that the initial electron transfer from CH_4 to CH_3OH species is the rate-determining step for MOR. Pure CuO_x at weak polarization region (low current density and overpotential) shows a low Tafel slope of 39 mV dec^{-1}, revealing how pure CuO_x could effectively improve the above rate-determining step. However, at strong polarization region, the Tafel slope of pure CuO_x increases, suggesting that the further oxidation of methane becomes difficult. By contrast, the capsule-like ZrO_2:$CuO_{x(180,24)}$ hybrid exhibited a lower Tafel slope (21 mV dec^{-1}) than CuO_x and ZrO_2, showing faster reaction kinetics for MOR. On the basis of the Tafel results and the previously reported work [4,25], a possible electrochemical mechanism for MOR to alcohols (1-propanol and 2-propanol) on the ZrO_2:$CuO_{x(180,24)}$ electrode was proposed (Fig. 2f). Initially, a CH_4 molecule is adsorbed on the surface of ZrO_2:CuO_x hybrid and then oxidized to generate CH_3OH and this step is identified as the rate-limiting step [37,50]. Then, the CH_3OH further oxidized to HCHO and finally to 2-propanol [22]. For 1-propanol, CH_4 binds to carbonate on the ZrO_2:CuO_x surface to produce CH_3·, which subsequently attacks CH_2CHOH and further generates the aim product according to the Markovnikov rule. This possible catalytic pathway is consistent with the Tafel slope result (21 mV dec^{-1}). The electrochemical reaction mechanism will be further discussed in DFT calculations and the analysis of MOR products.

3.3. DFT analysis

To gain mechanistic insights of the promoted electrocatalytic performance, two models of Cu_2O(111) and ZrO_2/Cu_2O(111), which consist of one ZrO_2 cluster adsorbed on the Cu_2O(111), are constructed to study the CH_4 dissociation processes and theoretically understand the higher activity of CH_4 oxidation to CH_3OH, as shown in Fig. 3**(a)** [51]. It is found that the CH_4 dissociates on the surface Cu site, forming CH_3 adsorbed on Cu atom and OH with neighbor O atom. For ZrO_2/Cu_2O

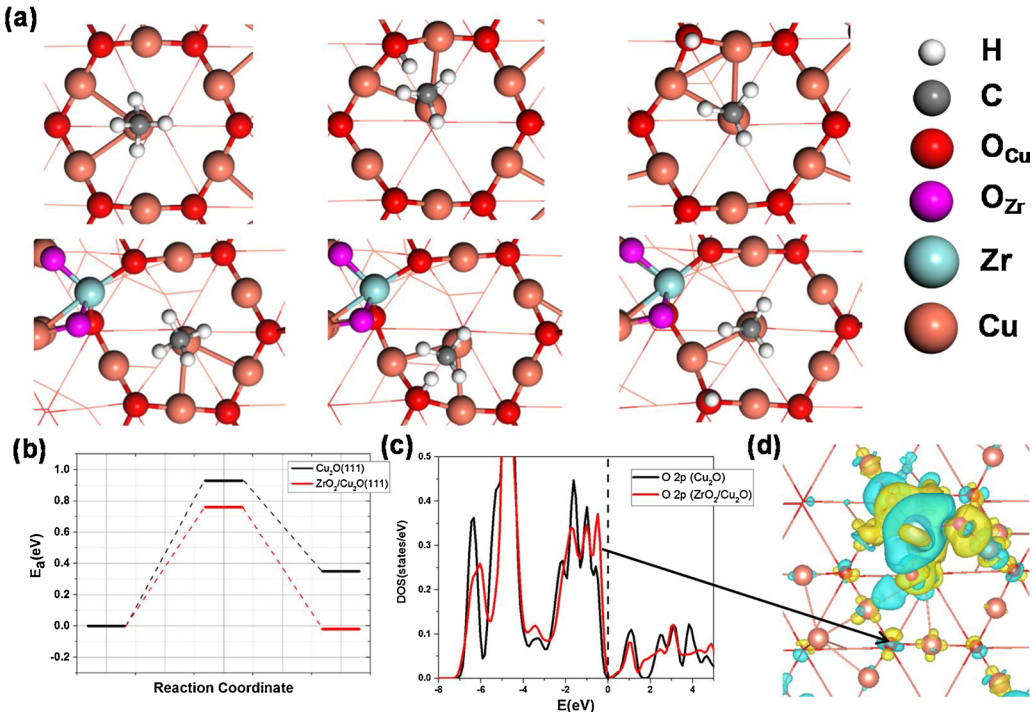

Fig. 3. (a) The CH_4 dissociation process for Cu_2O(111) and ZrO_2:Cu_2O(111). (b) The corresponding Ea vs Reaction coordinate, (c) the 2p density of states of surface O of the Fermi level, (d) the charge density difference of the ZrO_2:Cu_2O(111) system. Negative and positive values are represented in light blue and yellow, respectively. The isosurface value used is 0.002 e $Å^{-3}$ (For interpretation of the references to colour in this figure legend, the reader is referred to the web version of this article).

(111), the CH_4 dissociation energy decreased by 0.17 eV (0.76 vs 0.93 eV) and the reaction becomes exothermal by 0.02 eV from endothermic by 0.35 eV (Fig. 3**(b)**). In order to explore the mechanism from an electronic level, the charge density difference is plotted in the Fig. 3**(c)** and **(d)**. The charge redistribution is obviously found after the ZrO_2 adsorbed on the $Cu_2O(111)$, especially in the neighbor of the ZrO_2 cluster. The charge redistribution in Cu during CH_4 dissociation is negligible; while it is much more for the neighbor O. The 2p orbital of O gets electrons after the ZrO_2 cluster adsorbed on the $Cu_2O(111)$. Furthermore, we plot the 2p states of O before and after ZrO_2 adsorbed on the $Cu_2O(111)$. The 2p states of O in the $ZrO_2/Cu_2O(111)$ increase to near its Fermi level, indicating that $ZrO_2/Cu_2O(111)$ possesses good electronic conduction. Moreover, the conductivity is improved by forming the high-speed electron transfer network, which is due to the transfer of O from the Cu_2O to the ZrO_2. The findings are in good agreement with the EIS results. In the end, the activity enhancements for CH_4 dissociation stem from the activated surface O by the adsorbed ZrO_2 cluster. In addition, the large adsorption energy and charge transfer indicates the strong chemical adsorption of CH_3 on the Cu_2O (111) surface. Bader charge analysis shows that the CH3 gets 1.21 |e| from the Cu_2O substrate.

3.4. Product analysis

To further analyze the product of MOR, a home-made reactor was assembled (Fig. 4**(a)**). The ZrO_2:$CuO_{x(180,24)}$ was sprayed on the 1*2 cm^2 carbon paper with the loading of 2 mg cm^{-2} as the working electrode. Based on the LSV curve of ZrO_2:$CuO_{x(180,24)}$, the potential of 1.3 V was selected as the working potential for MOR. The potential not only helps the high oxidation current, but also benefits the low OER competition. The products of MOR in CH_4-saturated carbonate electrolyte were collected at 3 h, 6 h, 12 h and 18 h, respectively. For further comparison, the products of MOR in N_2-saturated electrolyte for 18 h were also collected. Here, ^{1}H-NMR spectroscopy was carried out to identify the products of MOR. As shown in Fig. 4**(b)**, 1-propanol and 2-propanol are the main oxidation products. In order to analyze the products, the concentration of various products of different reaction time measured by the GC–MS system is shown in Table 1. Five organic products are detected, including methanol, ethanol, acetaldehyde, 1-propanol, and 2-propanol. As displayed in Table 1, the amount of one-carbon atom compounds (methanol) are similar with reaction time, revealing a balance between consumption and production. The amount of ethanol increased with the reaction time, illustrating that ethanol is the main two-carbon product. In addition, the amount of acetaldehyde decreased with the reaction time. As detailed in a previous report [52], the acetaldehyde plays an important role in the generation of propanol. This finding further shows that the acetaldehyde might be a chemical intermediate of the conversion into 1-propanol and 2-propanol. After 18 h, 1-propanol and 2-propanol were the main stable products of CH_4 oxidation. The content of 1-propanol (2105.8 ug mL^{-1}) slightly exceeds that of 2-propanol (2084.3 ug mL^{-1}) at 18 h, even though 2-propanol has a higher thermodynamic stability [29]. The finding reveals ZrO_2:$CuO_{x(180,24)}$ has a unique selectivity for 1-propanol production through free radical addition in a carbonate electrolyte. Hence, the analysis of the products from CH_4 oxidation appears consistent with the above MOR mechanism shown in Fig. 2**(f)**. This indicated that it is suitable pathway of the free radical addition reaction as the main step in CH_4 electrochemical oxidation.

Table 1
Concentrations of various products after the electrochemical oxidation of CH_4 for 3, 6, 9 and 18 h.

Time (h)	Methanol (ug / mL)	Ethanol (ug / mL)	Acetaldehyde (ug / mL)	1-Propanol (ug / mL)	2-Propanol (ug / mL)
3	35.1	0	197.6	15.2	24.6
6	37.6	0	159.7	75.1	144.8
9	38.4	21.7	147.3	658.6	701.8
18	39.3	45.8	138.4	2105.8	2084.3

4. Conclusion

In summary, the capsule-like ZrO_2:CuO_x electrocatalyst was synthesized and used in CH_4 electrochemical oxidation at room temperature. The active sites are hypothesized to originate from CuO_x. The corresponding experimental and DFT results show that the high performance of the hybrid can be attributed to (i) the strong synergistic-coupling effect between CuO_x and ZrO_2; (ii) the unique morphology and structure, and (iii) the charge redistribution of ZrO_2:CuO_x. As expected, the hybrid shows high catalytic activity with a large Δj of 13.35 mA cm^{-2} and long-term stability. ZrO_2:CuO_x catalysts have a highly efficient oxidation-selective conversion of CH_4 to 1- and 2- propanol in a home-made reactor. The new design of the catalyst and the electrochemical pathway offer more possibilities for the synthesis of higher alcohols by CH_4 oxidation at room temperature.

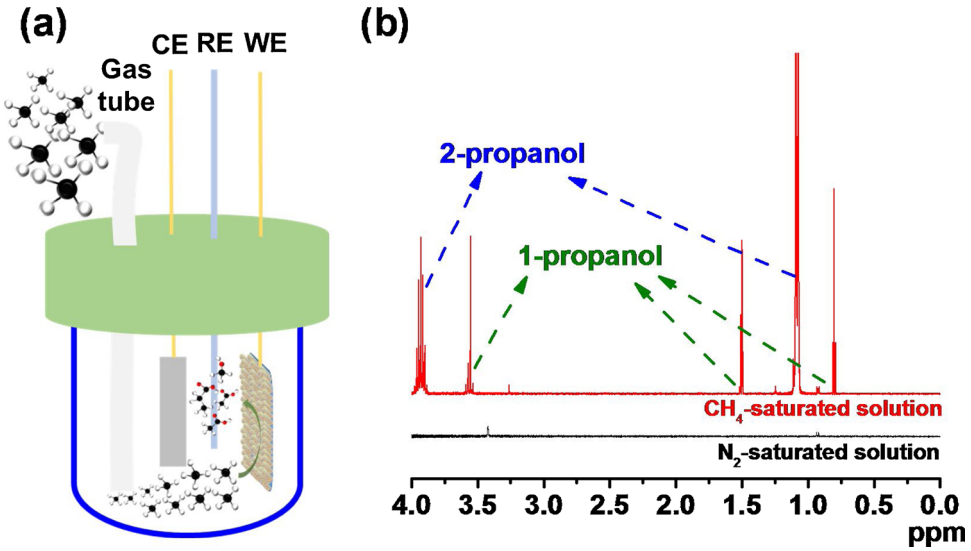

Fig. 4. (a) The scheme of the electrochemical oxidation reaction of methane gas. (b) 1H-NMR spectrum of the products after 18 h in CH_4- and N_2- saturated electrolyte.

CRediT authorship contribution statement

Nengneng Xu: Conceptualization, Writing - original draft. **Cameron A. Coco:** Formal analysis, Writing - review & editing. **Yudong Wang:** Methodology, Writing - original draft. **Tianshun Su:** Investigation. **Yu Wang:** Data curation. **Luwei Peng:** Investigation, Formal analysis. **Yanxing Zhang:** Methodology, Investigation, Writing - original draft. **Yuyu Liu:** Methodology, Writing - review & editing. **Jinli Qiao:** Methodology, Resources, Supervision, Validation, Writing - review & editing. **Xiao-Dong Zhou:** Conceptualization, Data curation, Funding acquisition, Project administration, Resources, Supervision, Writing - review & editing.

Declaration of Competing Interest

The authors declare no competing financial interests.

Acknowledgements

This material is based upon work supported by the National Science Foundation under Grant No. NSF-1747603. The authors would like to thank Ms. Jamie Malcombe for valuable discussion. CAC acknowledges the support from Board of Reagents under the contract of LEQSF(2017-22)-GF-20.

Appendix A. Supplementary data

Supplementary material related to this article can be found, in the online version, at doi:https://doi.org/10.1016/j.apcatb.2020.119572.

References

[1] Z. Jin, L. Wang, E. Zuidema, K. Mondal, M. Zhang, J. Zhang, C. Wang, X. Meng, H. Yang, C. Mesters, F.-S. Xiao, Hydrophobic zeolite modification for in situ peroxide formation in methane oxidation to methanol, Science 367 (2020) 193, https://doi.org/10.1126/science.aaw1108.

[2] C.T. Dinh, T. Burdyny, M.G. Kibria, A. Seifitokaldani, C.M. Gabardo, F.P. Garcia de Arquer, A. Kiani, J.P. Edwards, P. De Luna, O.S. Bushuyev, C. Zou, R. Quintero-Bermudez, Y. Pang, D. Sinton, E.H. Sargent, CO_2 electroreduction to ethylene via hydroxide-mediated copper catalysis at an abrupt interface, Science 360 (2018) 783–787, https://doi.org/10.1126/science.aas9100.

[3] W. Wang, C. Su, Y. Wu, R. Ran, Z. Shao, Progress in solid oxide fuel cells with nickel-based anodes operating on methane and related fuels, Chem. Rev. 113 (2013) 8104–8151, https://doi.org/10.1021/cr300491e.

[4] M. Ma, C. Oh, J. Kim, J.H. Moon, J.H. Park, Electrochemical CH_4 oxidation into acids and ketones on ZrO_2:$NiCo_2O_4$ quasi-solid solution nanowire catalyst, Appl. Catal. B: Environ. 259 (2019) 118095, https://doi.org/10.1016/j.apcatb.2019.118095.

[5] Y. Zhao, H. Wang, J. Han, X. Zhu, D. Mei, Q. Ge, Simultaneous activation of CH_4 and CO_2 for concerted C-C coupling at oxide-Oxide interfaces, ACS Catal. 9 (2019) 3187–3197, https://doi.org/10.1021/acscatal.9b00291.

[6] S.E. Temmel, E. Fabbri, D. Pergolesi, T. Lippert, T.J. Schmidt, Investigating the role of strain toward the oxygen reduction activity on model thin film Pt catalysts, ACS Catal. 6 (2016) 7566–7576, https://doi.org/10.1021/acscatal.6b01836.

[7] B. Lee, Y. Sakamoto, D. Hirabayashi, K. Suzuki, T. Hibino, Direct oxidation of methane to methanol over proton conductor/metal mixed catalysts, J. Catal. 271 (2010) 195–200, https://doi.org/10.1016/j.jcat.2010.01.011.

[8] S. Xie, S. Lin, Q. Zhang, Z. Tian, Y. Wang, Selective electrocatalytic conversion of methane to fuels and chemicals, J. Energy Chem. 27 (2018) 1629–1636, https://doi.org/10.1016/j.jechem.2018.03.015.

[9] A. Gremminger, P. Lott, M. Merts, M. Casapu, J.-D. Grunwaldt, O. Deutschmann, Sulfur poisoning and regeneration of bimetallic Pd-Pt methane oxidation catalysts, Appl. Catal. B: Environ. 218 (2017) 833–843, https://doi.org/10.1016/j.apcatb.2017.06.048.

[10] Q. Shen, C. Cao, R. Huang, L. Zhu, X. Zhou, Q. Zhang, L. Gu, W. Song, Single chromium atoms supported on titanium dioxide nanoparticles for synergic catalytic methane conversion under mild conditions, Angew. Chem. Int. Ed. Engl. 59 (2020) 1216–1219, https://doi.org/10.1002/anie.201913309.

[11] A. Tomita, J. Nakajima, T. Hibino, Direct oxidation of methane to methanol at low temperature and pressure in an electrochemical fuel cell, Angew. Chem. Int. Ed. Engl. 47 (2008) 1462–1464, https://doi.org/10.1002/anie.200703928.

[12] A. Gremminger, J. Pihl, M. Casapu, J.-D. Grunwaldt, T.J. Toops, O. Deutschmann, PGM based catalysts for exhaust-gas after-treatment under typical diesel, gasoline and gas engine conditions with focus on methane and formaldehyde oxidation, Appl. Catal. B: Environ. 265 (2020) 118571, https://doi.org/10.1016/j.apcatb.2019.118571.

[13] B. Wang, S. Albarracín-Suazo, Y. Pagán-Torres, E. Nikolla, Advances in methane conversion processes, Catal. Today 285 (2017) 147–158, https://doi.org/10.1016/j.cattod.2017.01.023.

[14] J.C.S. Araújo, L.F. Oton, B. Bessa, A.B.S. Neto, A.C. Oliveira, R. Lang, L. Otubo, J.M.C. Bueno, The role of Pt loading on La_2O_3-Al_2O_3 support for methane conversion reactions via partial oxidation and steam reforming, Fuel 254 (2019) 115681, https://doi.org/10.1016/j.fuel.2019.115681.

[15] X. Shi, Y. Shuai, F. Wang, C. Zhang, Z. Cheng, X. Chen, Effects of ordered hierarchically porous structure on methane reforming performance in solar foam reactor, J. Co2 Util. 37 (2020) 147–157, https://doi.org/10.1016/j.jcou.2019.12.002.

[16] S. Bai, F. Liu, B. Huang, F. Li, H. Lin, T. Wu, M. Sun, J. Wu, Q. Shao, Y. Xu, X. Huang, High-efficiency direct methane conversion to oxygenates on a cerium dioxide nanowires supported rhodium single-atom catalyst, Nat. Commun. 11 (2020) 954, https://doi.org/10.1038/s41467-020-14742-x.

[17] K. Huang, J.B. Miller, G.W. Huber, J.A. Dumesic, C.T. Maravelias, A general framework for the evaluation of direct nonoxidative methane conversion strategies, Joule 2 (2018) 349–365, https://doi.org/10.1016/j.joule.2018.01.001.

[18] K. Villa, S. Murcia-López, T. Andreu, J.R. Morante, Mesoporous WO_3 photocatalyst for the partial oxidation of methane to methanol using electron scavengers, Appl. Catal. B: Environ. 163 (2015) 150–155, https://doi.org/10.1016/j.apcatb.2014.07.055.

[19] Z. Li, X. Pan, Z. Yi, Photocatalytic oxidation of methane over CuO-decorated ZnO nanocatalysts, J. Mater. Chem. A 7 (2019) 469–475, https://doi.org/10.1039/C8TA09592B.

[20] Z. Boukha, A. Choya, M. Cortés-Reyes, B. de Rivas, L.J. Alemany, J.R. González-Velasco, J.I. Gutiérrez-Ortiz, R. López-Fonseca, Influence of the calcination temperature on the activity of hydroxyapatite-supported palladium catalyst in the methane oxidation reaction, Appl. Catal. B: Environ. 277 (2020) 119280, https://doi.org/10.1016/j.apcatb.2020.119280.

[21] G. Li, Y. Fang, C. Arges, C. Plaisance, J. Flake, Communication-electrocatalytic coupling of methane at platinum oxide electrodes in Superacids, J. Electrochem. Soc. 167 (2020) 155503, https://doi.org/10.1149/1945-7111/aba704.

[22] N. Agarwal, S.J. Freakley, R.U. McVicker, S.M. Althahban, N. Dimitratos, Q. He, D.J. Morgan, R.L. Jenkins, D.J. Willock, S.H. Taylor, C.J. Kiely, G.J. Hutchings, Aqueous Au-Pd colloids catalyze selective CH_4 oxidation to CH_3OH with O_2 under mild conditions, Science 358 (2017) 223–227, https://doi.org/10.1126/science.aan6515.

[23] Z. Guo, W. Chen, Y. Song, X. Dong, G. Li, W. Wei, Y. Sun, Efficient methane electrocatalytic conversion over a Ni-based hollow fiber electrode, Chinese J. Catal. 41 (2020) 1067–1072, https://doi.org/10.1016/s1872-2067(20)63548-3.

[24] Y. Amenomiya, V.I. Birss, M. Goledzinowski, J. Galuszka, A.R. Sanger, Conversion of methane by oxidative coupling, Catal. Rev. 32 (1990) 163–227, https://doi.org/10.1080/01614949009351351.

[25] N. Spinner, W.E. Mustain, Electrochemical methane activation and conversion to oxygenates at room temperature, J. Electrochem. Soc. 160 (2013) F1275–F1281, https://doi.org/10.1149/2.071311jes.

[26] N. Spinner, W.E. Mustain, Influence of non-conducting zirconia on the electrochemical performance of nickel oxide in alkaline media at room temperature, J. Electrochem. Soc. 159 (2012) E187–E192, https://doi.org/10.1149/2.051212jes.

[27] B. Samaranch, P. Ramírez de la Piscina, G. Clet, M. Houalla, P. Gélin, N. Homs, Synthesis and characterization of Ta_2O_5-ZrO_2 systems: structure, surface acidity, and catalytic properties, Chem. Mater. 19 (2007) 1445–1451, https://doi.org/10.1021/cm062704z.

[28] D. Lehninger, D. Rafaja, J. Wünsche, F. Schneider, J. von Borany, J. Heitmann, Formation of orthorhombic $(Zr,Ta)O_2$ in thin Zr-Ta-O films, Appl. Phys. Lett. 110 (2017) 262903, https://doi.org/10.1063/1.4990529.

[29] M. Ma, B.J. Jin, P. Li, M.S. Jung, J.I. Kim, Y. Cho, S. Kim, J.H. Moon, J.H. Park, Ultrahigh electrocatalytic conversion of methane at room temperature, Adv. Sci. 4 (2017) 1700379, https://doi.org/10.1002/advs.201700379.

[30] L. Zhao, J. Zhao, T. Wu, M. Zhao, W. Yan, Y. Zhang, H. Li, Y. Wang, T. Xiao, Y. Zhao, Synergistic effect of oxygen vacancies and Ni species on tuning selectivity of Ni/ZrO_2 catalyst for hydrogenation of maleic anhydride into succinic anhydride and gamma-butyrolacetone, Nanomaterials 9 (2019) 9030406, https://doi.org/10.3390/nano9030406.

[31] O.A. Baturina, Q. Lu, M.A. Padilla, L. Xin, W. Li, A. Serov, K. Artyushkova, P. Atanassov, F. Xu, A. Epshteyn, T. Brintlinger, M. Schuette, G.E. Collins, CO_2 electroreduction to hydrocarbons on carbon-supported Cu nanoparticles, ACS Catal. 4 (2014) 3682–3695, https://doi.org/10.1021/cs500537y.

[32] Y. Huang, A.D. Handoko, P. Hirunsit, B.S. Yeo, Electrochemical reduction of CO_2 using copper single-crystal surfaces: effects of CO* coverage on the selective formation of ethylene, ACS Catal. 7 (2017) 1749–1756, https://doi.org/10.1021/acscatal.6b03147.

[33] Y.X. Duan, F.L. Meng, K.H. Liu, S.S. Yi, S.J. Li, J.M. Yan, Q. Jiang, Amorphizing of Cu nanoparticles toward highly efficient and robust electrocatalyst for CO_2 reduction to liquid fuels with high faradaic efficiencies, Adv. Mater. 30 (2018) 1706194, https://doi.org/10.1002/adma.201706194.

[34] K. Larmier, W.C. Liao, S. Tada, E. Lam, R. Verel, A. Bansode, A. Urakawa, A. Comas-Vives, C. Coperet, CO_2-to-methanol hydrogenation on zirconia-supported copper nanoparticles: reaction intermediates and the role of the metal-support interface, Angew. Chem. Int. Ed. Engl. 56 (2017) 2318–2323, https://doi.org/10.1002/anie.201610166.

[35] K. Jiang, R.B. Sandberg, A.J. Akey, X. Liu, D.C. Bell, J.K. Nørskov, K. Chan, H. Wang, Metal ion cycling of Cu foil for selective C–C coupling in electrochemical CO_2 reduction, Nat. Catal. 1 (2018) 111–119, https://doi.org/10.1038/s41929-017-0009-x.

[36] S. Tada, K. Larmier, R. Büchel, C. Copéret, Methanol synthesis via CO_2 hydrogenation over CuO-ZrO_2 prepared by two-nozzle flame spray pyrolysis, Catal. Sci. Technol. 8 (2018) 2056–2060, https://doi.org/10.1039/c8cy00250a.
[37] Z. Liu, E. Huang, I. Orozco, W. Liao, R.M. Palomino, N. Rui, T. Duchoň, S. Nemšák, D.C. Grinter, M. Mahapatra, P. Liu, J.A. Rodriguez, S.D. Senanayake, Water-promoted interfacial pathways in methane oxidation to methanol on a CeO_2-Cu_2O catalyst, Science 368 (2020) 513–517, https://doi.org/10.1126/science.aba5005.
[38] K.T. Dinh, M.M. Sullivan, K. Narsimhan, P. Serna, R.J. Meyer, M. Dincă, Y. Román-Leshkov, Continuous partial oxidation of methane to methanol catalyzed by diffusion-paired copper dimers in copper-exchanged zeolites, J. Am. Chem. Soc. 141 (2019) 11641–11650, https://doi.org/10.1021/jacs.9b04906.
[39] Z. Riguang, L. Hongyan, L. Lixia, L. Zhong, W. Baojun, A DFT study on the formation of CH_3O on Cu_2O(111) surface by CH3OH decomposition in the absence or presence of oxygen, Appl. Surf. Sci. 257 (2011) 4232–4238, https://doi.org/10.1016/j.apsusc.2010.12.026.
[40] T. Ikuno, S. Grundner, A. Jentys, G. Li, E. Pidko, J. Fulton, M. Sanchez-Sanchez, J.A. Lercher, Formation of active Cu-oxo clusters for methane oxidation in Cu-Exchanged mordenite, J. Phys. Chem. C 123 (2019) 8759–8769, https://doi.org/10.1021/acs.jpcc.8b10293.
[41] H. Oguchi, H. Kanai, K. Utani, Y. Matsumura, S. Imamura, Cu_2O as active species in the steam reforming of methanol by CuO/ZrO_2 catalysts, Appl. Catal. A Gen. 293 (2005) 64–70, https://doi.org/10.1016/j.apcata.2005.07.010.
[42] K.V. Chary, G.V. Sagar, C.S. Srikanth, V.V. Rao, Characterization and catalytic functionalities of copper oxide catalysts supported on zirconia, J. Phys. Chem. B 111 (2007) 543–550, https://doi.org/10.1021/jp063335x.
[43] F. Diao, F. Tian, W. Liang, H. Feng, Y. Wang, Mechanistical investigation on the self-enhanced photocatalytic activity of CuO/Cu_2O hybrid nanostructures by density functional theory calculations, Phys. Chem. Chem. Phys. 18 (2016) 27967–27975, https://doi.org/10.1039/c6cp03977d.
[44] D. Pietrogiacomi, M.C. Campa, L.R. Carbone, S. Tuti, M. Occhiuzzi, N_2O decomposition on CoO_x, CuO_x, FeO_x or MnO_x supported on ZrO_2: the effect of zirconia doping with sulfates or K^+ on catalytic activity, Appl. Catal. B: Environ. 187 (2016) 218–227, https://doi.org/10.1016/j.apcatb.2016.01.018.
[45] A.F. Zedan, A.S. AlJaber, Combustion synthesis of non-precious CuO-CeO_2 nanocrystalline catalysts with enhanced catalytic activity for methane oxidation, Materials 12 (2019), https://doi.org/10.3390/ma12060878.
[46] S. Raveendran, S. Kannan, Polymorphism and phase transitions in t-ZrO_2/$CoFe_2O_4$ composite structures: impact of composition and heat treatments, Cryst. Growth Des. 19 (2019) 4710–4720, https://doi.org/10.1021/acs.cgd.9b00583.
[47] B. Liu, Y. Li, S. Qing, K. Wang, J. Xie, Y. Cao, Engineering CuO_x-ZrO_2-CeO_2 nanocatalysts with abundant surface Cu species and oxygen vacancies toward high catalytic performance in CO oxidation and 4-nitrophenol reduction, CrystEngComm 22 (2020) 4005–4013, https://doi.org/10.1039/D0CE00588F.
[48] W. Wang, Z. Qu, L. Song, Q. Fu, CO_2 hydrogenation to methanol over Cu/CeO_2 and Cu/ZrO_2catalysts: tuning methanol selectivity via metal-support interaction, J. Energy Chem. 40 (2020) 22–30, https://doi.org/10.1016/j.jechem.2019.03.001.
[49] N. Xu, J.A. Wilson, Y.-D. Wang, T. Su, Y. Wei, J. Qiao, X.-D. Zhou, Y. Zhang, S. Sun, Flexible self-supported bi-metal electrode as a highly stable carbon- and binder-free cathode for large-scale solid-state zinc-air batteries, Appl. Catal. B: Environ. 272 (2020) 118953, , https://doi.org/10.1016/j.apcatb.2020.118953.
[50] C.C. Chang, C.Y. Liu, Y.C. Sun, Effective methane conversion to methanol on bifunctional graphene-oxide-supported platinum nanoclusters (Pt5)-a DFT study, Phys. Chem. Chem. Phys. 22 (2020) 4967–4973, https://doi.org/10.1039/c9cp06002b.
[51] K. Harrath, X. Yu, H. Xiao, J. Li, The key role of support surface hydrogenation in the CH4 to CH3OH selective oxidation by a ZrO_2-supported single-atom catalyst, ACS Catal. 9 (2019) 8903–8909, https://doi.org/10.1021/acscatal.9b02093.
[52] I. Bar-Nahum, A.M. Khenkin, R. Neumann, Mild, aqueous, aerobic, catalytic oxidation of methane to methanol and acetaldehyde catalyzed by a supported bipyrimidinylplatinum-polyoxometalate hybrid compound, J. Am. Chem. Soc. 126 (2004) 10236–10237, https://doi.org/10.1021/ja0493547.